Journal of Applied Fluid Mechanics, Vol. 18, No. 8, pp. 2026-2042, 2025.
Available online at www.jafmonline.net, ISSN 1735-3572, EISSN 1735-3645.
https://doi.org/10.47176/jafm.18.8.3278

Rapid Prediction of Ice Accretion on Swept Wings Based on Proper Orthogonal Decomposition and Surrogate Modelling

J. Du[1], Q. Guo[1,2†], Y. Yue[1,2], Y. Ma[1,2] and H. Cheng[1]

[1] *Civil Aviation Flight University of China, Guanghan, Sichuan, 618307, China*
[2] *Key Laboratory of Flight Techniques and Flight Safety, CAAC, Guanghan, Sichuan, 618307, China*

†*Corresponding Author Email: guoql@cafuc.edu.cn*

ABSTRACT

Numerical simulations of three-dimensional airfoil icing are computationally intensive, with icing complexities on swept wings surpassing those on straight wings. To enable rapid and accurate ice formation predictions on swept wings, this study proposes a prediction methodology integrating proper orthogonal decomposition (POD) and Kriging surrogate modelling. This approach incorporates key physical parameters influencing ice formation, including flight altitude, flight speed, ambient temperature, liquid water content, and median volume diameter. First, an optimized Latin hypercube sampling method (OLHS) was employed to generate 120 icing conditions under both continuous and intermittent maximum icing scenarios. Numerical simulations were then conducted to establish an icing dataset, which was subsequently transformed into one-dimensional ice height data for various two-dimensional airfoil sections. Next, surrogate models for two-dimensional airfoils were developed using POD and Kriging interpolation to establish relationships between meteorological and flight conditions and the corresponding icing shapes. Finally, three-dimensional ice geometries were reconstructed through uniform interpolation of multiple two-dimensional icing profiles. Validation results demonstrated a strong agreement between surrogate model predictions and numerical simulations, enabling rapid and accurate real-time ice shape estimations across various conditions. The predicted ice shape similarity exceeded 94% for rime ice and 89% for glaze ice. This methodology provides valuable insights for aircraft anti-icing and de-icing design while also contributing to the development of optimized ice-tolerant aerodynamic strategies.

Article History

Received December 8, 2024
Revised February 17, 2025
Accepted March 10, 2025
Available online June 3, 2025

Keywords:

Aircraft icing
Swept wings
Ice shape prediction
Proper orthogonal decomposition
Kriging

1. INTRODUCTION

Aircraft icing has long been recognised as a significant threat to flight safety. This phenomenon occurs when supercooled water droplets in clouds collide with the wing surface, resulting in ice accretion. The accumulation of ice on the airfoil can adversely affect an aircraft's aerodynamic performance (Kim & Bragg, 1999), leading to an increase in drag, a decrease in lift (Olsen et al., 1984), and, in severe cases, a complete loss of control.

In recent years, intensified climate change and the increasing frequency of extreme weather events have significantly heightened the occurrence and severity of aircraft icing in certain regions, presenting ongoing challenges to aviation safety, particularly on flight routes susceptible to ice accretion (Ryley et al., 2020). According to the NTSB, 228 icing-related accidents occurred between 2006 and 2010 (Appiah et al., 2013). Although modern aircraft are equipped with de-icing and anti-icing systems, complete eradication of in-flight icing remains unachievable. To address this issue, global regulatory agencies, including the Federal Aviation Administration (2004), Civil Aviation Administration of China (2011), and the European Union Aviation Safety Agency (2016), have implemented airworthiness regulations to ensure comprehensive safety assessments across various icing conditions. However, existing countermeasures have not entirely mitigated these risks. Therefore, further research on the dynamics of aircraft icing is essential to enhance risk mitigation strategies and improve flight safety.

NOMENCLATURE

a	subscript, air	β	droplet collection efficiency
f	subscript, film	E	total internal energy
ρ	density	κ	thermal conductivity coefficient
t	time variable	c	specific heat capacity
δ	identity tensor	Re	Reynolds number
$\boldsymbol{g}$	gravity acceleration	Fr	local Froude number
v	velocity components.	h	thickness
H	enthalpy	T_e	equilibrium temperature at the air/film/wall/ice
α	mean droplet concentration	c_h	convective heat transfer coefficient
K	inertial parameter	m_{evap}	evaporation or sublimation mass flux
C_d	droplet drag coefficient	L_{evap}	latent heat of evaporation or sublimation
T	temperature	$\boldsymbol{U}$	linearly independent vectors
$\boldsymbol{\tau}$	the shear stress	$\boldsymbol{b}$	vector coefficients
ε	surface emissivity	λ	eigenvalue
$T_{ice,rec}$	recovered temperature of ice	$\boldsymbol{Y}$	response value
m_{ice}	instantaneous mass accumulation of ice	θ	correlation parameter
L_{fusion}	evaporation or sublimation	$\hat{\boldsymbol{\beta}}$	global trend
$Q_{anti-icing}$	anti-icing heat flux	ϖ	weights
$\boldsymbol{\Phi}$	orthonormal basis functions	X_{mt}	maximum ice thickness
$\boldsymbol{\Psi}$	eigenvector	X_{iw}	impact width
$\boldsymbol{X}$	parameter variable	X_{hl}	horn length
$\boldsymbol{r}$	correlation vector	X_{lowlm}	lower limit positions
ϖ^2	overall variance	X_{lowha}	upper horn angle
$\boldsymbol{R}$	correlation matrix	X_{lowhl}	upper horn length
X_{st}	ice thickness at the stagnation point	S_{ave}	average area
X_{mw}	maximum ice width	Rat	ice shape difference rate
X_{ha}	horn angle	b	span
X_{uplm}	upper limit positions	**ABBREVIATION**	
X_{upha}	upper horn angle	POD	Proper Orthogonal Decomposition
X_{uphl}	upper horn length	LWC	Liquid Water Content
S_{dif}	area of the non-overlapping parts	FAA	Federal Aviation Administration
Dav	mean characteristic difference rate	EASA	Civil Aviation Administration Of China
Par	ice shape similarity	SWIM	Shallow-Water Icing Model
d	subscript, droplet	SIMPLE	Semi-Implicit Method For Pressure-Linked Equations
s	subscript, solid	OLHS	Optimal Latin Hypercube Sampling
$\boldsymbol{V}$	velocity	MVD	Median Volume Diameter
σ	stress tensor	CAAC	Civil Aviation Administration Of China
μ	viscosity coefficient	FVM	Finite Volume Method
p	static pressure		

Comprehensive aerodynamic assessments of ice-accreted airfoils are essential for accurately evaluating the impact of icing on aircraft performance. Currently, the primary methods for studying aircraft icing include experimental and numerical simulation techniques (Yi, 2007). Experimental approaches, such as ice wind tunnel tests and in-flight trials, provide direct results and serve as a critical foundation for the design and certification of aircraft and engine anti-icing systems (Li et al., 2022). However, their high cost, extended timelines, and limited generalizability constrain their widespread application.

Recent advances in numerical simulations have provided effective alternatives for studies requiring high reproducibility and iterative testing (Milani et al., 2024). However, accurately modelling the icing process remains computationally demanding due to the intricate calculations involved in airflow fields, droplet impact characteristics, icing modules, and mesh iterations, all of which contribute to significant computational costs and extended processing times (Aliaga et al., 2011; Olejniczak & Nowacki 2018; Dai et al., 2021). As a result, improving computational efficiency while maintaining the accuracy of icing prediction has become a primary focus of current research. Yi et al. (2021) developed an aircraft icing prediction model based on deep belief networks and stacked autoencoders, demonstrating the capability to accurately capture the nonlinear behaviour of aircraft icing. Suo et al. (2024) developed an airfoil icing prediction model based on geometrical constraint enhancement neural networks, significantly improving the accuracy of icing predictions. Chang et al. (2016) introduced a prediction model that integrates wavelet packet transform and artificial neural networks to estimate ice accretion. Li et al. (2020) conducted a rapid assessment of maximum ice thickness, icing area, and icing severity using machine learning techniques based on XGBoost. Abdelghany et al. (2023) proposed a method based on machine learning and the Internet of Things to predict the thermal performance characteristics of wing anti-icing systems. They developed surrogate models capable of rapidly predicting icing-related data under different operating conditions.

Surrogate models serve as approximate mathematical representations that replace complex and computationally intensive numerical analyses (Han, 2016). These models enable the rapid evaluation of complex system behaviours, significantly reducing computational time, particularly for large-scale simulations or evaluations (Forrester et al., 2008). When constructing a surrogate model for aircraft icing analysis, it is crucial to capture icing variations across the entire design space. Direct numerical simulations of icing are often time consuming and costly, requiring a large initial sample size to ensure model accuracy. The proper orthogonal decomposition (POD) method effectively reduces computational complexity by decomposing multidimensional data and mapping key features into a lower-dimensional space while preserving the primary system dynamics. Given the highly nonlinear nature of aircraft icing, the POD method decomposes the factors influencing icing into characteristic basis vectors, transforming complex icing data into coefficient samples for surrogate model training. This surrogate model then establishes a relationship between data-space sampling points and fitting parameters, enabling rapid and efficient predictions of ice formation on airfoil surfaces.

POD and surrogate methods have been widely applied in various fields, including aerodynamic shape optimisation (Zhao et al., 2022), airflow prediction (Min, 2024), and the rapid estimation of anti-icing thermal loads (Bu et al., 2017). Jung et al. (2011) integrated POD with surrogate models to account for multiple icing factors, effectively predicting droplet collection efficiency and ice accretion shapes. Pellissier et al. (2012) improved an anti-icing cavity layout based on genetic algorithms, POD, and Kriging methods. Shen et al. (2013) developed a rapid ice-shape prediction algorithm based on POD, achieving fast predictions under triparametric variations. Liu et al. (2019) combined POD with a Kriging-based surrogate model for rapid ice shape predictions across multiple parameters and conducted comparative analyses of different kriging models. More recently, Niu et al. (2023) developed POD and Kriging surrogate models to represent ice shapes over time, enabling effective prediction of time-dependent ice accretion and aerodynamic characteristics. Currently, wing icing prediction primarily relies on two-dimensional numerical simulations. However, these simulations exhibit limitation in accurately predicting icing on three-dimensional swept wings, particularly due to pressure gradient variations along the span and vortex flow at the wingtips, both of which significantly influence ice formation and accretion. The unique aerodynamic design of swept wings introduces complex airflow characteristics and boundary layer behaviours, further complicating precise icing prediction. Therefore, there is an urgent need to develop an efficient and precise icing prediction model capable of rapidly assessing icing risks on three-dimensional airfoils under diverse climatic conditions to enhance flight safety.

This study presents a rapid prediction method for icing on swept wings using POD and surrogate modelling. Initially, the OLHS method was employed to generate 120 icing conditions under both continuous and intermittent maximum icing scenarios. Numerical simulations conducted under these conditions produced an icing dataset, which was subsequently converted into one-dimensional ice height data for different 2D sections. Surrogate models were then developed for multiple 2D sections using POD combined with kriging interpolation. To enable fast and accurate 3D icing predictions on swept wings, uniform interpolation was applied across these sections. Validation tests under various icing conditions demonstrated that the proposed method effectively predicted ice accretion on swept wings.

2. METHOD

2.1 Ice Accretion Numerical Simulation

Ice accretion numerical simulation involves calculating the airflow field, droplet impingement characteristics, thermodynamic icing processes, and mesh reconstruction. The airflow field distribution was determined by solving the Navier–Stokes equations using the finite volume method (FVM), with the semi-implicit method for pressure-linked equations (SIMPLE) applied to ensure accurate pressure-velocity coupling. The droplet impingement characteristics were calculated using the Eulerian two-phase flow method, and ice formation was then predicted based on the Messinger thermodynamic model.

2.1.1 Airflow Field Calculation

Fluid flow must adhere to three fundamental physical conservation laws: mass conservation, momentum conservation, and energy conservation. When the airflow field is turbulent, additional turbulent transport equations must also be satisfied. The mass conservation law is expressed as follows (Habashi, 2003):

$$\frac{\partial \rho_a}{\partial t} + \boldsymbol{\nabla} \cdot \left(\rho_a \boldsymbol{V}_a \right) = 0 \tag{1}$$

Here, ρ_a represents the air density, V_a denotes the air velocity, t is a time variable.

For a Newtonian fluid, the law of momentum conservation states that the net force acting on a fluid particle is equal to the rate of change of its momentum over time. The momentum conservation law is expressed as:

$$\frac{\partial \rho_a \boldsymbol{V}_a}{\partial t} + \boldsymbol{\nabla} \cdot \left(\rho_a \boldsymbol{V}_a \boldsymbol{V}_a \right) = \boldsymbol{\nabla} \cdot \sigma^{ij} + \rho_a \boldsymbol{g} \tag{2}$$

$$\sigma^{ij} = -\delta^{ij} p_a + \tau^{ij} \tag{3}$$

$$\tau^{ij} = \mu_a \left[\delta^{jk} \nabla_k v^i + \delta^{ik} \nabla_k v^j - \frac{2}{3} \delta^{ij} \nabla_k v^k \right] \tag{4}$$

where σ represents the stress tensor, g is the gravitational acceleration, p_a is the static pressure, δ is the identity tensor, μ_a is the viscosity coefficient, τ represents the viscous stress tensor, and v^i, v^j, and v^k are the velocity components.

The law of energy conservation states that the total energy of a system remains constant, meaning that its energy input and output must be equal. The energy conservation law is expressed as:

$$\begin{aligned} &\frac{\partial \rho_a E_a}{\partial t} + \boldsymbol{\nabla} \cdot \left(\rho_a \boldsymbol{V}_a H_a \right) = \\ &\boldsymbol{\nabla} \cdot \left(\kappa_a \left(\boldsymbol{\nabla} T_a \right) + v_i \tau^{ij} \right) + \rho_a \boldsymbol{g} \cdot \boldsymbol{V}_a \end{aligned} \tag{5}$$

Here, E represents the total internal energy, H denotes the enthalpy, and κ_a is the thermal conductivity coefficient.

2.1.2 Droplet Impact Analysis

The motion trajectories of supercooled droplets were calculated using the Eulerian two-phase flow model to determine droplet impingement characteristics (Bourgault et al., 1999). The governing equations used are as follows:

$$\frac{\partial \alpha}{\partial t} + \boldsymbol{\nabla} \cdot \left(\alpha \boldsymbol{V}_d \right) = 0 \tag{6}$$

$$\begin{aligned} &\frac{\partial \left(\alpha \boldsymbol{V}_d \right)}{\partial t} + \boldsymbol{\nabla} \left[\alpha \boldsymbol{V}_d \otimes \boldsymbol{V}_d \right] = \\ &\frac{C_D Re_d}{24K} \alpha \left(\boldsymbol{V}_a - \boldsymbol{V}_d \right) + \alpha \left(1 - \frac{\rho_a}{\rho_d} \right) \frac{1}{Fr^2} \end{aligned} \tag{7}$$

where α is the mean droplet concentration, and $\vec{V}_d$ denotes the mean droplet velocity. The first term on the right side of Eq. (7) corresponds to the drag force exerted on the particles, which is proportional to the relative velocity between the droplets and the surrounding airflow. The second term accounts for the combined effects of buoyancy and gravity forces acting on the droplets.

2.1.3 Ice Accretion Model

After obtaining the droplet impingement characteristics, the SWIM was developed based on the Messinger model (Bourgault et al., 2015). Figure 1 illustrates the heat and mass transfer phenomena occurring within a thin water film on the aircraft surface. During the runback process, the film undergoes phase changes, including freezing, sublimation, or evaporation, depending on the local thermodynamic conditions.

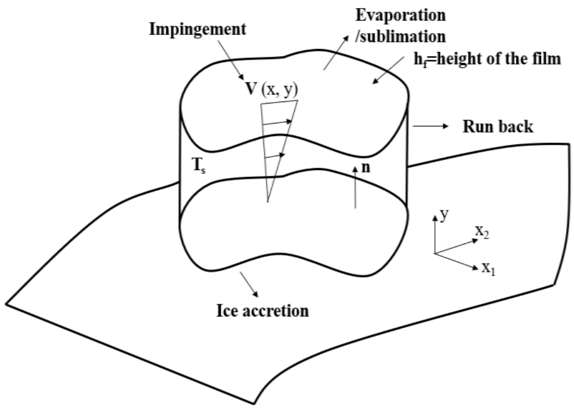

Fig. 1 Heat and mass balance in a thin film

The function of $\boldsymbol{x}$ and y is the film velocity, that y is the coordinate normal to the surface. and $\boldsymbol{x}$ is the coordinate along the surface. The film velocity is assumed to have a linear distribution due to the extremely thin nature of the water film. The velocity can be calculated as follows:

$$\boldsymbol{V}_f \left(\boldsymbol{x}, y \right) = \frac{y}{\mu_f} \boldsymbol{\tau}_{a,wall} \left(\boldsymbol{x} \right) \tag{8}$$

Here, $\boldsymbol{\tau}_{a,wall}$ is the shear stress of air. The average velocity can be calculated as:

$$\boldsymbol{V}_f \left(\boldsymbol{x}, y \right) = \frac{1}{h_f} \int_0^{h_f} \boldsymbol{V}_f \left(\boldsymbol{x}, y \right) dy = \frac{h_f}{2\mu_f} \boldsymbol{\tau}_{a,wall} \left(\boldsymbol{x} \right) \tag{9}$$

Here, h_f is the film thickness. The following is the mass conservation equation:

$$\rho_f \left[\frac{\partial h_f}{\partial t} + \vec{\nabla} \cdot \left(\boldsymbol{V}_f h_f \right) \right] = V_\infty LWC \beta - \dot{m}_{evap} - \dot{m}_{ice} \tag{10}$$

Where the terms on the right of Eq. (10) represent the masses due to droplet impingement, evaporation, and ice accumulation, respectively. The following is the energy conservation equation:

$$\begin{aligned} &\rho_f \left[\frac{\partial h_f c_f \tilde{T}_e}{\partial t} + \vec{\nabla} \cdot \left(\bar{V}_f h_f c_f \tilde{T}_e \right) \right] = \\ &\left[c_f \left(\tilde{T}_\infty - \tilde{T}_e \right) + \frac{\left\| \boldsymbol{V}_d \right\|^2}{2} \right] V_\infty LWC \beta - L_{evap} \dot{m}_{evap} \\ &+ \left(L_{fusion} - c_s \tilde{T} \right) \dot{m}_{ice} + \sigma \varepsilon \left(T_\infty^4 - T_e^4 \right) \\ &- c_h \left(\tilde{T}_e - \tilde{T}_{ice,rec} \right) + Q_{anti-icing} \end{aligned} \tag{11}$$

where the first three terms on the right-hand side represent the heat transfer contributions from water droplets impinging, evaporation, and ice accumulation, respectively. The last three terms represent the heat transfer due to radiation, convection, and conduction. The specific meanings of the symbols are provided in the nomenclature table.

2.2 POD and Surrogate Model

2.2.1 POD

The POD method extracts key features from high-dimensional data by reconstructing the physical field using a linear superposition of orthogonal basis functions. In the design space Ω, a set of linearly independent vectors $\left\{\boldsymbol{U}^{(i)}\right\}\Big|_{i=1}^{k}$ is chosen, where the elements of these vectors are referred to as "snapshots" (Sirovich, 1987). Within the space spanned by these snapshots, a set of orthonormal basis functions, $\left\{\boldsymbol{\Phi}^{(i)}\right\}\Big|_{i=1}^{k}$ is constructed, such that the projection of the elements onto the orthogonal basis is maximised. The formula is given by:

$$\begin{cases} \max\limits_{\boldsymbol{\Phi}} \dfrac{1}{k}\sum\limits_{i=1}^{k}\left|\left(\boldsymbol{U}^{(i)},\boldsymbol{\Phi}\right)\right|^2 \\ \left(\boldsymbol{\Phi},\boldsymbol{\Phi}\right)=1 \end{cases} \tag{12}$$

The orthonormal basis functions $\left\{\boldsymbol{\Phi}^{(i)}\right\}\Big|_{i=1}^{k}$ can be represented as a linear superposition of the snapshots:

$$\boldsymbol{\Phi}^{(i)}=\sum_{i=1}^{k}\boldsymbol{b}_j^{(i)}\boldsymbol{U}^{(i)} \tag{13}$$

where $\boldsymbol{b}_j^{(i)}$ is the vector coefficient. Once these coefficients are obtained, the orthonormal basis of $\boldsymbol{\Phi}^{(i)}$ can be determined. The distinct eigenvalues of the matrix arranged in descending order are $\left(\lambda^{(1)},\lambda^{(2)},\lambda^{(3)}...\lambda^{(k)}\right)$, The eigenvector corresponding to the eigenvalue is denoted as $\boldsymbol{\Psi}^{(i)}=\left[\Psi_1^i\Psi_2^i...\Psi_k^i\right]^T$, The i-th orthonormal basis is given by:

$$\boldsymbol{\Phi}^{(i)}=\sum_{i=1}^{k}\boldsymbol{\Psi}_j^{(i)}\boldsymbol{U}^{(i)} \tag{14}$$

The size of the eigenvalue represents the energy contribution of each fundamental function to the entire set. Accordingly, the fundamental functions can be truncated to reconstruct the physical field. The energy of the truncated subspace must closely approximate that of the original vector space to ensure an accurate representation of the system's dominant features.

$$\sum_{i=1}^{M}\lambda^{(i)}\Big/\sum_{j=1}^{N}\lambda^{(j)}\approx 1 \tag{15}$$

2.2.2 Kriging Surrogate Model

The core idea of the kriging surrogate model is to construct an efficient surrogate model using existing observational data, enabling prediction and optimisation without directly computing a complex real model.

Before using the Kriging surrogate model, n input parameter sampling points $\left\{\boldsymbol{X}^{(i)}\right\}\Big|_{i=1}^{n}$ must be collected, along with their corresponding system response values $\left\{\boldsymbol{Y}^{(i)}\right\}\Big|_{i=1}^{n}$, where each $\boldsymbol{X}^{(i)}$ is a n-dimensional vector. The surrogate model assumes that the true relationship between the system response and the design variables is expressed as (Qiu, 2013):

$$F\left(\boldsymbol{X}\right)=f\left(\boldsymbol{X}\right)+z\left(\boldsymbol{X}\right) \tag{16}$$

Here, $\boldsymbol{X}$ is a parameter variable, and $f\left(\boldsymbol{X}\right)$ is a global approximate model, that represents the deterministic part. $z\left(\boldsymbol{X}\right)$ is a stochastic process with a mean value of 0.

The correlation of the objective function was determined by the spatial distance between the sample points. The Gaussian correlation function is defined as:

$$r\left(\left\|\boldsymbol{X}-\boldsymbol{X}'\right\|\right)=exp\left(-\sum_{k=1}^{n}\theta_k\left|\boldsymbol{X}_k-\boldsymbol{X}_k'\right|^2\right) \tag{17}$$

Here, $\left\|\boldsymbol{X}-\boldsymbol{X}'\right\|$ represents the distance between sample point $\boldsymbol{X}$ and $\boldsymbol{X}'$. θ_k is the correlation parameter of direction k .The correlation vector between the input point and the sampling point is denoted as $\boldsymbol{r}\left(\boldsymbol{X}\right)$. The correlation matrix is $\boldsymbol{R}$.

$$\boldsymbol{r}\left(\boldsymbol{X}\right)=\left[r\left(\left\|\boldsymbol{X}-\boldsymbol{X}_1\right\|\right),...,r\left(\left\|\boldsymbol{X}-\boldsymbol{X}_n\right\|\right)\right]^T \tag{18}$$

$$\boldsymbol{R}_{ij}=r\left(\left\|\boldsymbol{X}_i-\boldsymbol{X}_j\right\|\right) \tag{19}$$

The global trend $\hat{\boldsymbol{\beta}}$ and weights ϖ are calculated using the following formulas.

$$\hat{\boldsymbol{\beta}}=\frac{\boldsymbol{I}^T\boldsymbol{R}^{-1}\boldsymbol{Y}}{\boldsymbol{I}^T\boldsymbol{R}^{-1}\boldsymbol{I}} \tag{20}$$

$$\varpi=\boldsymbol{R}^{-1}\left(\boldsymbol{Y}-\hat{\boldsymbol{\beta}}\boldsymbol{I}\right) \tag{21}$$

Here, $\boldsymbol{I}$ is a vector in which all elements are equal to one. $\boldsymbol{Y}$ is an objective function of a sampling point.

The key to constructing the kriging surrogate model is determining the optimal weight vector. The hyperparameters were optimised by maximising the likelihood function. A genetic algorithm was employed to determine the optimal vector θ .

$$\begin{aligned}\log L\left(\theta\right)&=-\frac{n}{2}\log\left(2\pi\omega^2\right)-\frac{1}{2}\log\left|\boldsymbol{R}\right| \\ &-\frac{1}{2\omega^2}\left(\boldsymbol{Y}-\hat{\boldsymbol{\beta}}\boldsymbol{I}\right)^T\boldsymbol{R}^{-1}\left(\boldsymbol{Y}-\hat{\boldsymbol{\beta}}\boldsymbol{I}\right)\end{aligned} \tag{22}$$

Here, ω^2 represents the overall variance of the objective function. After obtaining the optimal vector, the estimated value corresponding to any new input parameter vector $\boldsymbol{X}_q$ is as follows:

$$F\left(\boldsymbol{X}_q\right)=\hat{\boldsymbol{\beta}}+\boldsymbol{r}^T\left(\boldsymbol{X}_q\right)\boldsymbol{R}^{-1}\left(\boldsymbol{Y}-\hat{\boldsymbol{\beta}}\boldsymbol{I}\right) \tag{23}$$

2.3 Coordinate Transformation and Ice Shape Similarity Assessment

2.3.1 Coordinate Transformation

The ice shape coordinate data points are typically represented in the Cartesian coordinate system, where their positions are determined by the x- and y-axis values. In this context, determining the coordinates of a point relies on a two-dimensional dataset. However, in surrogate models, the required sample size increases exponentially with the number of input dimensions. This makes it challenging for the surrogate model to effectively capture the relationship between inputs and outputs, ultimately affecting prediction accuracy. To mitigate this issue, dimensionality reduction techniques or optimised sampling strategies can be employed to enhance model accuracy and computational efficiency.

A coordinate transformation method is employed to map the Cartesian coordinate system to the ξ-η coordinate system (Zhang, 2016). This transformation involves preserving the wing surface arc length coordinate points and reducing the two-dimensional Cartesian coordinate data to one-dimensional ice height data, thereby enhancing the efficiency and accuracy of the surrogate model. The detailed transformation process is outlined as follows.

After obtaining the ice-shape data in the Cartesian coordinate system, the leading-edge stagnation point of the clean airfoil is designated as the origin of the coordinate system. The surface arc length, denoted as ξ, is used as the horizontal coordinate, where the arc length along the upper surface is positive, and that along the lower surface is negative. The starting and ending points of the airfoil surface correspond to the upper and lower points at the maximum thickness of the airfoil, respectively. The vertical coordinate η represents the direction of the airfoil surface's outer normal. The distance from the intersection of the outer normal and the ice shape to the airfoil surface is defined as the ice height, thereby establishing the ξ-η coordinate system. Figure 2 illustrates the coordinate transformation process.

In this study, a structured grid was used for the 3D swept wings. Consequently, the number of ice-shaped curve data points varied under different icing conditions in the 2D sections. However, the node data of the clean airfoil remained consistent. To standardize the dataset, the clean airfoil curve data were used as a reference, and airfoil data points before 0.3 times the chord length were selected, resulting in a total of 193 grid nodes. At each grid node, the outer normal intersects with the ice shape curve, and the distance between the grid node and the intersection point is defined as the ice height. Ultimately, only the ice height data for various operating conditions must be predicted.

2.3.2 Ice Shape Feature Parameters

Ruff and Anderson (2003). proposed an ice shape feature parameter method to quantitatively characterize ice shape profiles and evaluate the accuracy of ice accretion predictions. This method provides a systematic approach to assessing ice formation on aerodynamic surfaces. An illustration of the ice-shaped characteristic parameters is shown in Fig. 3.

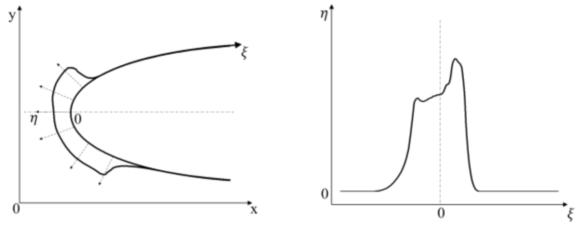

(a) Cartesian coordinate system (b) ξ-η coordinate system

Fig. 2 Coordinate transformation process

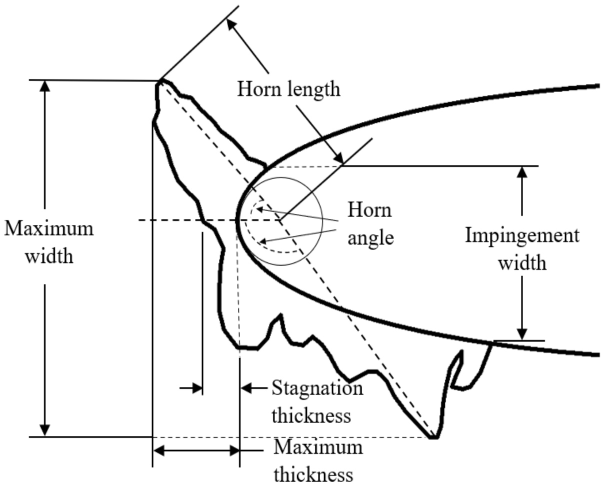

Fig. 3 Ice Shape characteristic parameters

Ice shape feature parameters include the ice thickness at the stagnation point X_{st} , maximum ice thickness X_{mt} , maximum ice width X_{mw} , impact width X_{iw} 、 horn angle X_{ha} and horn length X_{hl} . The impact width X_{iw} can be further divided into the upper X_{uplm} and lower limit positions X_{lowlm} , Similarly, horn angle X_{ha} can be categorized into upper horn angle X_{upha} and lower horn angle X_{lowha} , while the horn length X_{hl} can be divided into upper horn length X_{uphl} and lower horn length X_{lowhl} .

2.3.3 Ice Shape Similarity Evaluation

The ice shape similarity assessment method proposed by Zhou et al. (2016) was employed to quantitatively evaluate the predicted ice shape and assess the accuracy of the surrogate model. This method utilizes the mean characteristic difference rate Dav , and the ice shape difference rate Rat to quantify the similarity between different ice shapes Par . The Dav primarily reflects the differences in macroscopic geometric characteristics of various ice formations. The calculation formulae are as follows:

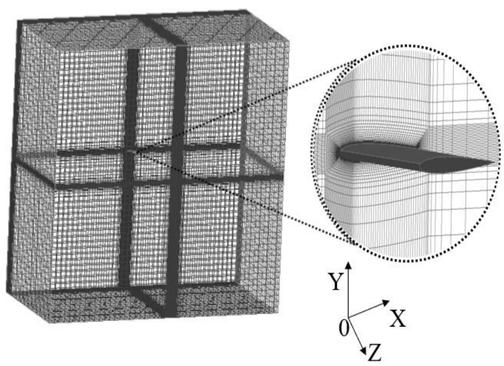

Fig. 4 Gird diagram of NACA 0012 straight wing

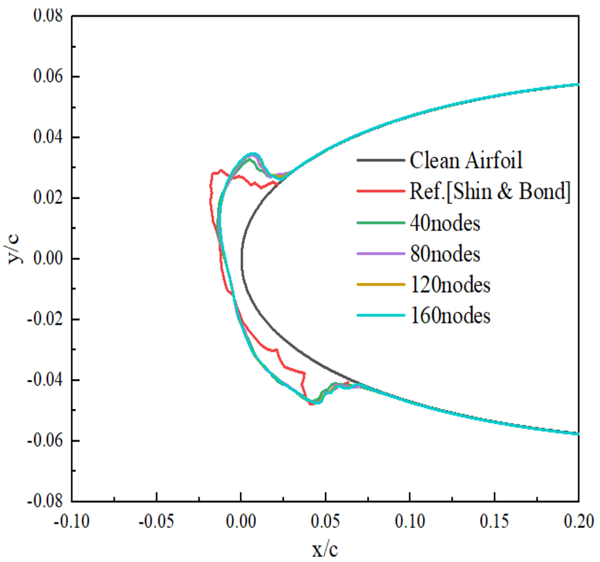

Fig. 5 Comparison of ice shapes at different grid nodes in condition V3

$$Dav = \sum_{i=1}^{n} \left| \frac{X_i - x_i}{n \cdot x_i} \right| \times 100\% \tag{24}$$

Here, X_i and x_i represent the geometric features of the predicted ice shape and the target ice shape, respectively. For rime ice, $n = 5$, which is represented by X_{st}, X_{mt}, X_{mw}, X_{uplm} and X_{lowlm}, respectively. For glaze ice, $n = 9$, with four additional ice shape features compared to rime ice, namely X_{upha}, X_{lowha}, X_{uphl} and X_{lowhl} 。

Rat primarily represents the rate of difference between different ice shapes, as follows:

$$Rat = \frac{S_{dif}}{S_{ave}} \tag{25}$$

Here, S_{dif} represents the area of the non-overlapping regions between the two ice shapes, while S_{ave} represents the average area of the two ice shapes.

To effectively assess the similarity between the two ice shapes, both variables must be considered. The ice shape similarity can be calculated using the following weighted formula:

Table 1 Typical verification Conditions Parameters

No	V, m/s	T, K	LWC, g/m^3	MVD, μm	t, s
V1	67.06	244.8	1.0	20	360
V2	102.8	262.4	1.8	30	360
V3	67.06	262.4	1.0	20	360

$$Par = r \cdot (1 - Dav) + (1 - r) \cdot (1 - Rat) \tag{26}$$

Where r is the weighting factor, and $r = 0.7$.

3. VALIDATION OF NUMERICAL SIMULATION

To validate the accuracy of the established numerical icing model, a three-dimensional simulation of ice accretion on the NACA0012 airfoil was conducted. The validation process included simulations for both rime and glaze ice, following the experimental conditions specified by Shin and Bond (1992) at the NASA Lewis Research Center. For these cases, the NACA0012 airfoil, with a chord length of 0.5334 m and a specified span $b = 0.5334m$ was modelled at a fixed angle of attack of 4°. The numerical simulation process was applied using the specific simulation parameters listed in Table 1. Figure. 4 presents the three-dimensional mesh of the NACA0012 straight wing, which consists of a total of 1.06 million mesh points. The mesh achieved a minimum quality of 0.68 and a mesh angle of 34.3°. The computational domain length was set to 18 times the chord length, with boundary conditions defined as five pressure far fields and one symmetry plane.

The numerical simulation results for icing were compared across different node distributions in the main icing regions, as shown in Fig. 5. Grids with 40, 80, 120, and 160 nodes were selected. For the grid with 40 nodes, the ice shape exhibited noticeable fluctuations, whereas for grids with other node counts, the variations were minimal. After balancing accuracy and efficiency, a grid with 80 nodes was selected for subsequent calculations.

The ice shape at the midsection of the airfoil (0.5 span) was compared with the experimental data from Shin and Bond (1992). Figure 6 presents a comparison of the ice shapes obtained from experimental results and numerical simulations for the two validation conditions. In this figure, the black line indicates the clean airfoil, while the blue and red lines correspond to the ice shapes derived from experimental data and numerical simulation, respectively. The numerically simulated ice shape demonstrated strong agreement with the experimental results, particularly in the overall profile. Figure 7 shows a comparison of the ice height curves for the two validation conditions. Under the rime ice condition, minor discrepancies are observed in the lower half of the ice height curve, whereas the upper half aligns closely with experimental data, indicating a strong overall ice match in ice shape. In the glaze ice condition, the simulation did not capture the small peak near the lower boundary; however, the overall ice shape remained largely consistent. Overall, the established

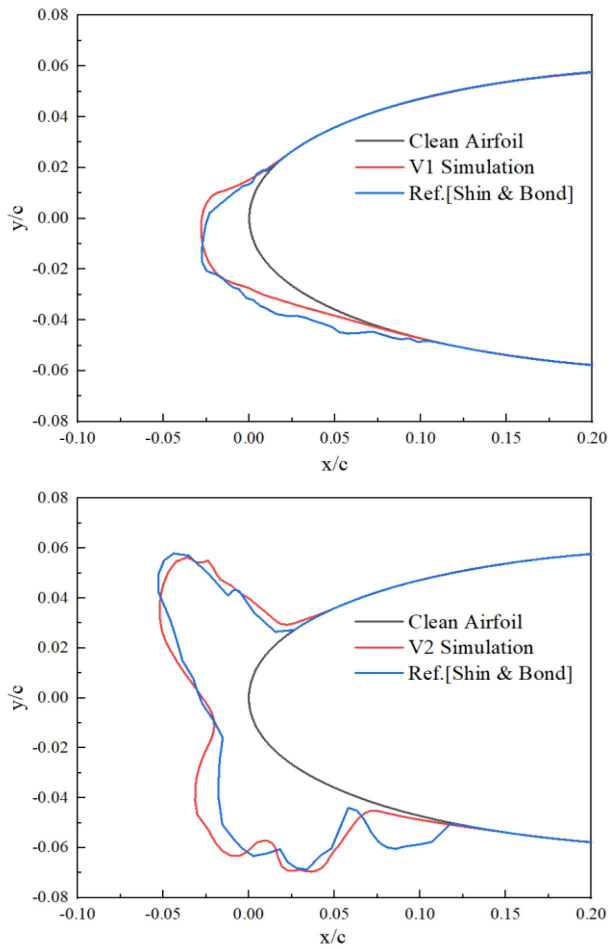

Fig. 6 Evaluation of ice shape between experimental results and numerical simulations

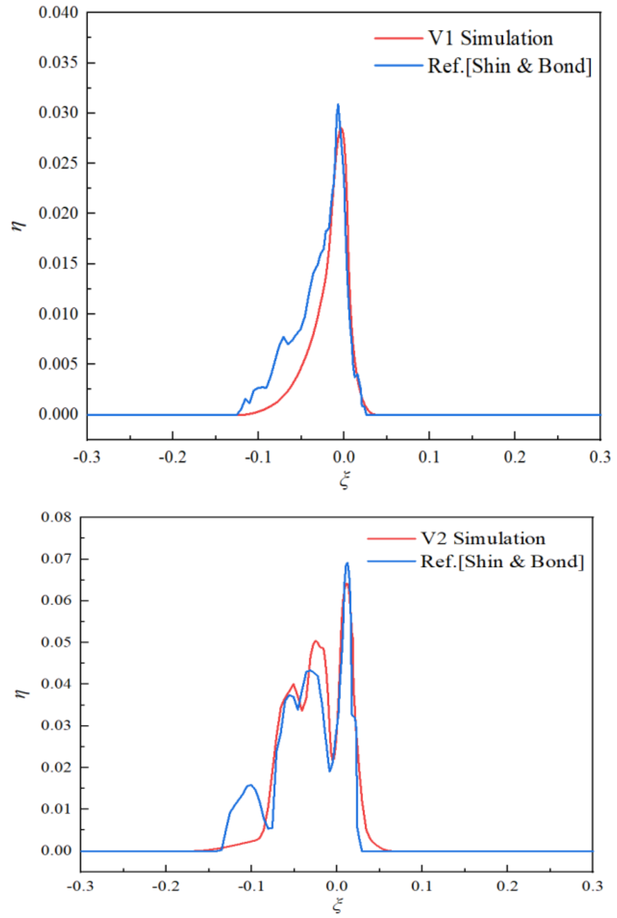

Fig. 7 Evaluation of ice height between experimental results and numerical simulation

numerical icing model effectively captured key features, including the ice shape, horn formation, and thickness, with only minor deviations near the ice boundaries.

For both the rime ice case (V1) and glaze ice case (V2), the *Par* value exceeded 85%, indicating a high level of consistency in the predicted ice shape. The *Dav* remained within 10%, demonstrating that the error was maintained within an acceptable range. The primary icing characteristics of glaze ice that adversely affect aerodynamic performance are the horn location and icing width. The shape feature difference rate for these two parameters was within 5%, ensuring that their impacts on aerodynamic performance remained relatively consistent. An aerodynamic performance degradation analysis for the glaze ice shape revealed a drag coefficient of 0.2339, compared to 0.2135 for the experimental ice shape, resulting in a relative error rate of 9.56%. These results indicate that the established numerical icing model effectively approximates the actual ice shape.

4. Results And Discussion

A swept-wing model based on the NACA0012 airfoil, incorporating a sweep angle of 30°, was applied to the icing simulation using the established numerical model. All other parameters remained consistent with those outlined in the previous section. Figure 8 shows the top

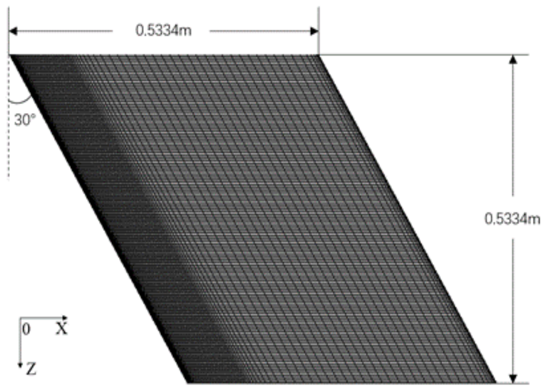

Fig. 8 Gird diagram of NACA 0012 swept wing

view of the swept-wing mesh used in the simulation. The introduction of a sweep angle adds aerodynamic complexity, influencing boundary layer characteristics and ice accretion behaviour. Therefore, this study provides a comprehensive validation of the model's predictive capabilities for swept-wing icing.

4.1 Ice Accretion Parameter Analysis

The primary factors influencing ice accretion shape include flight speed, LWC, MVD, and ambient temperature. To analyse the impact of these parameters on ice formation, a multi-parameter study was conducted.

Table 2 Icing environment baseline parameters

T, K	V, m/s	t, s	LWC, g/m^3	MVD, □m
263.15	80	360	1.0	25

The reference values for the icing parameters are provided in Table 2. For this analysis, an ice-shaped cross section at the mid-span location (0.5 span) of the swept wing was selected.

Figure 9 presents a comparison of ice shapes under varying icing parameters. The influence of ambient temperature on ice accretion is illustrated in Fig. 9(a). When the ambient temperature exceeded 263.15 K, glaze ice was formed, characterised by distinct ice horns. At 268.15 K, the droplets flowed rearward along the airfoil surface, leading to a runback ice phenomenon. At the critical temperature of 263.15 K, the ice shape exhibited ice horn features but closely resembled rime ice, representing a transitional state between rime and glaze ice. Below this critical temperature, the icing type remained as rime ice, and further decreases in temperature did not significantly alter the ice shape.

Figure 9(b) compares the ice shapes at different flight speeds. At lower flight speeds, the ice formation resembled rime ice, as the droplets froze immediately upon impact with the wing, resulting in minimal droplet flow along the airfoil surface. As flight speed increased, the rate of ice accretion also increased. At higher speeds, the icing type transitioned from rime to glaze ice, characterised by the formation of ice horns. Additionally, both the extent and thickness of ice accretion increased, with the ice horn becoming more pronounced. However, as flight speed continued to increase, the increment in stagnation thickness gradually decreased, ultimately approaching zero.

The ice shapes under varying LWC levels are compared in Fig. 9 (c). At lower LWC, rime ice formed as supercooled droplets froze immediately upon contact with the wing. As LWC increased, the ice type transitioned to glaze ice, with the ice horn feature becoming more pronounced. Once the icing transitioned to glaze ice, further increases in LWC led to larger ice horns, longer ice formations, and greater ice thicknesses at the stagnation point, while the upper and lower icing limits remained relatively stable. The icing rate was directly proportional to LWC.

The ice shapes for different MVD are compared in Fig. 9(d). At lower MVD, rime ice forms, whereas higher MVD values result in the transition to glaze ice with ice horn features. As the MVD increased, the droplets exhibited greater inertia, leading to an expansion of both the upper and lower icing limits, as well as an increase in ice horn size and length. However, the ice thickness at the stagnation point remained largely unchanged.

In conclusion, glaze ice formation predominated at higher flight speeds, ambient temperatures, LWC, and MVD, whereas rime ice was more common at lower values of these parameters. Among these factors, ambient temperature had the most significant impact on the icing type. The flight speed and LWC primarily influenced the icing rate, ice horn characteristics, and stagnation point ice

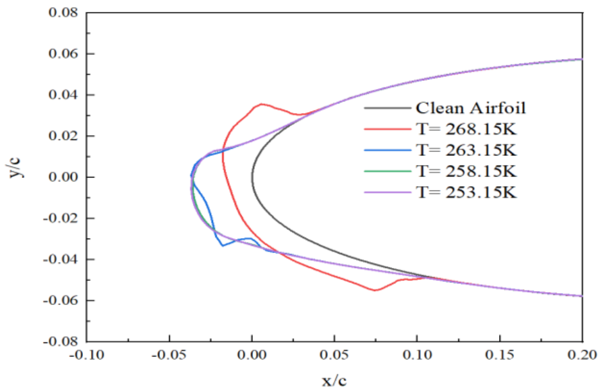

(a) Different ambient temperatures

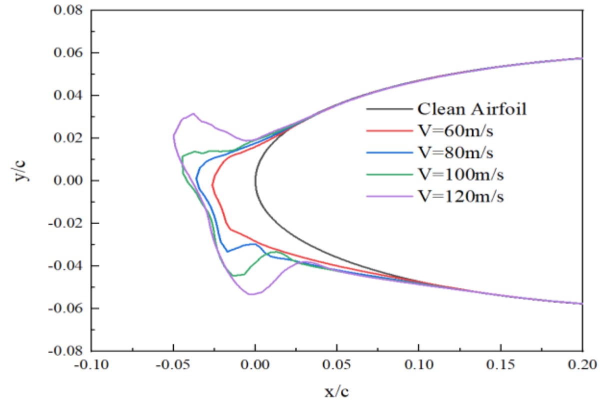

(b) Different flight speeds

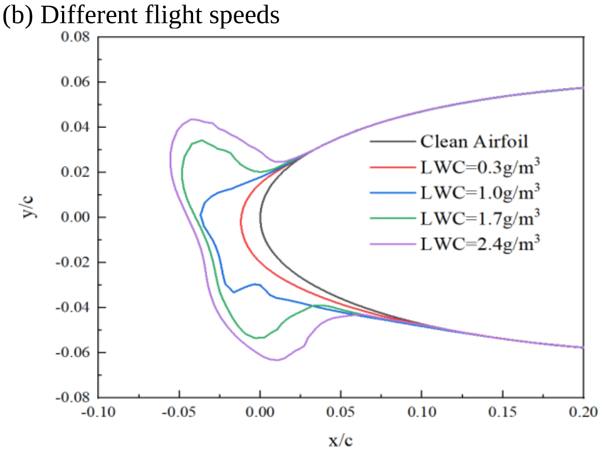

(c) Different LWC

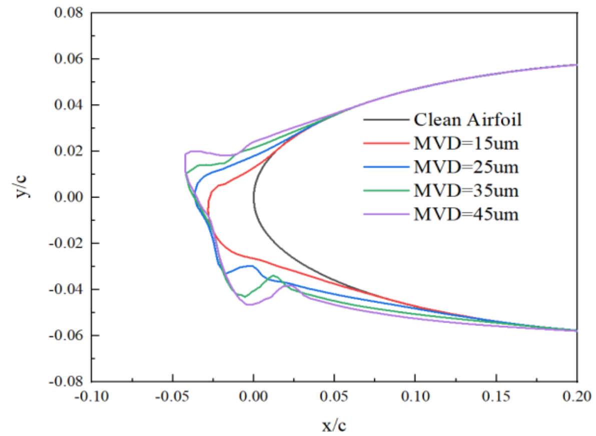

(d) Different MVD

Fig. 9 Comparison of ice shapes under different icing parameters

Table 3 Validation parameters of intermittent and continuous maximum icing conditions

Icing condition	No	V, m/s	H, km	T, K	LWC, g/m^3	MVD, μm
Continuous maximum	1	59	3.1	258	0.2	29
	2	62	2.4	255	0.35	17
	3	83	2.2	253	0.22	19.5
	4	87	3.5	269	0.53	20
Intermittent maximum	5	75	4.8	240	0.3	37
	6	115	3	259	2.2	17
	7	102	5	257	1.3	24
	8	93	3.9	262	0.72	33

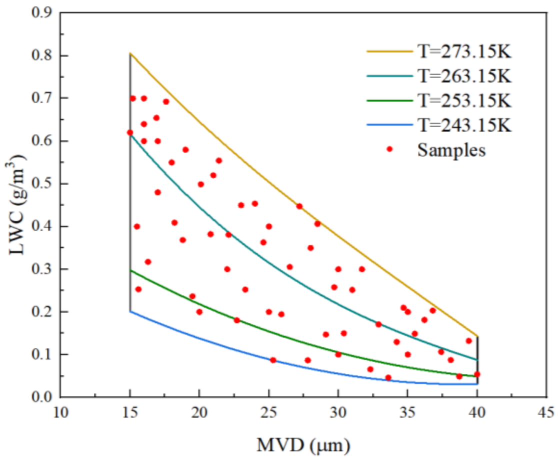

(a) Continuous maximum icing conditions

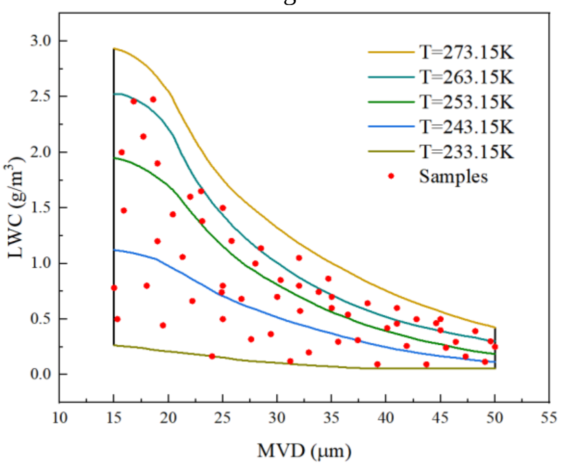

(b) Intermittent maximum icing conditions

Fig. 10 Samples of continuous/intermittent maximum icing conditions

thickness. The environmental temperature mainly affected both the ice horn formation and stagnation point ice thickness. Meanwhile, MVD primarily influenced the upper and lower icing limits, ice horn features, and icing accumulation rate.

4.2 Ice Accretion Prediction Surrogate Model

The continuous maximum icing conditions and intermittent maximum icing conditions are defined in Appendix C of FAR Part 25. Using the OLHS, 60 sampling conditions were generated for each icing scenario, and the distribution of these sampling points is shown in Fig. 10. The inflow speed ranged from 50 to 120 m/s, with an icing duration of 600 s for continuous maximum icing conditions and 300 s for intermittent maximum icing conditions. Icing simulations were conducted at these 120 sampling points to analyse the ice shapes under varying conditions. Building on this framework, coordinate transformations were applied to convert Cartesian coordinates into ξ-η coordinates. Surrogate models were developed using POD and Kriging interpolation, incorporating five key icing parameters: flight speed, altitude, ambient temperature, LWC, and MVD. These models were employed to predict icing height data at unsampled points, which were then transformed back into Cartesian coordinates for comparison with the simulated ice shapes. Table 3 presents the validation parameters of continuous and intermittent maximum icing conditions

Figure 11 evaluates the ice shapes predicted by the surrogate model with those obtained from numerical simulations under continuous maximum icing conditions. Validation conditions 1–3 resulted in rime ice formation, whereas condition 4 exhibited glaze ice characteristics. The comparison of ice shapes demonstrates that the surrogate model predictions for conditions 1–3 closely match the numerical simulations. Both the overall ice profile and accretion trends were consistent, with high similarity in icing thickness, as well as in the upper and lower icing limits. For Condition 4, the predicted icing thickness closely aligned with the numerical results. However, slight deviations were observed in the lengths of the upper and lower ice horns, along with minor discrepancies in the lower limit position. Overall, the rapid prediction algorithm provided accurate predictions across all four validation conditions under continuous maximum icing. It effectively captured the icing curves, with minor discrepancies primarily occurring in regions with high curvature, particularly near the ice horns.

Figure 12 presents a comparison between the predicted and simulated icing shapes under intermittent maximum icing conditions. Among the four validation cases, Case 5 corresponds to rime ice, while Cases 6–8 correspond to glaze ice. The ice shapes predicted by the surrogate model for Case 6 exhibited a high degree of overlap with the numerically simulated ice shapes, demonstrating strong predictive accuracy. In Case 7, a slight discrepancy was observed in the ice horn length; however, the overall ice shape profile remained consistent with the simulation results. For Case 8, minor deviations were noted in the upper and lower limits, as well as in the upper ice horn angle. Despite these differences, the overall ice shape remained in good agreement with the numerical simulations.

For the rime ice case, the predicted ice shape closely aligned with the simulated result, with similar icing feature parameters. In glaze ice cases, the rapid prediction algorithm accurately captured the overall icing limits and ice height curves. However, some discrepancies were observed in the upper and lower ice horns. The simulated ice-shape exhibited more complex curvature changes, while the rapid prediction algorithm predicted a smoother curve. This suggests that the model has minor limitations in capturing finer geometric details.

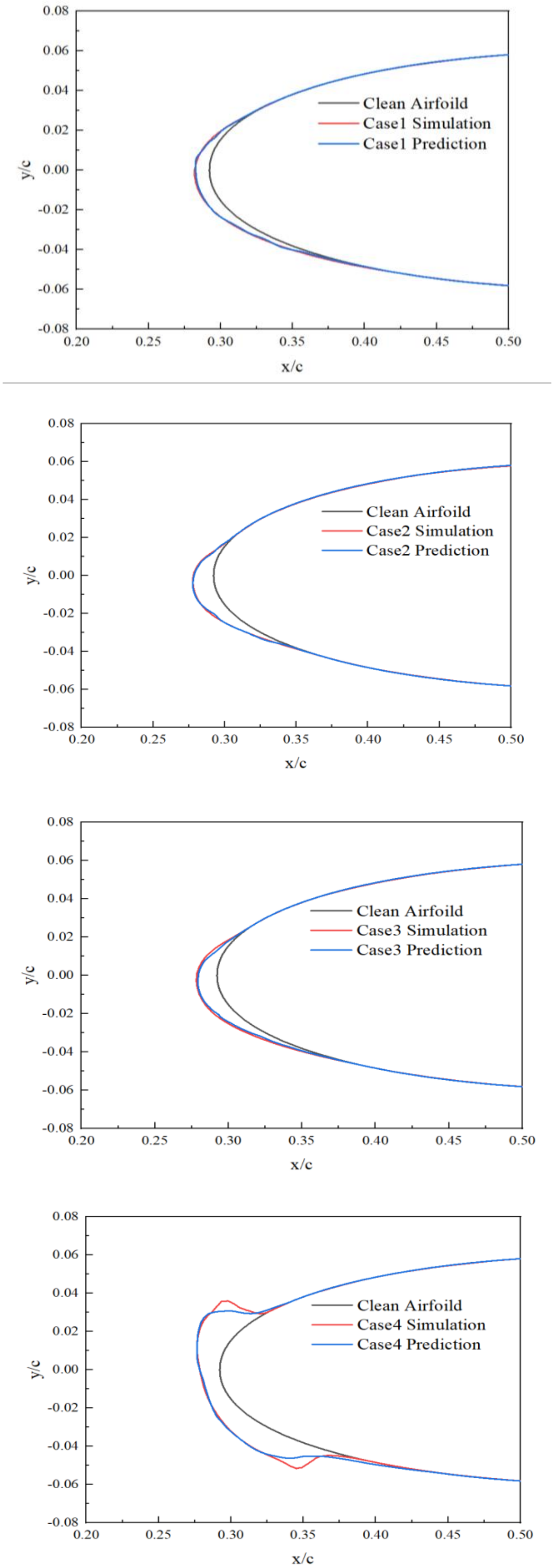

Fig. 11 Comparison of predicted and simulated icing shapes for validation conditions under continuous maximum icing conditions

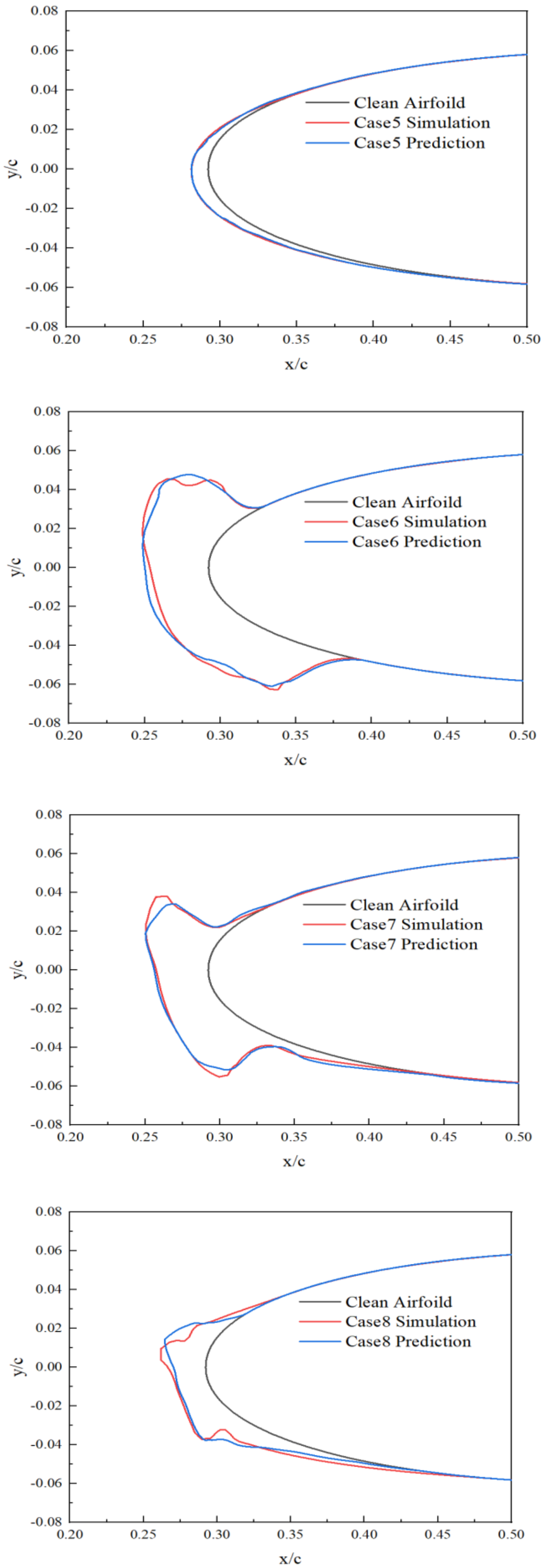

Fig. 12 Comparison of predicted and simulated icing shapes for validation conditions under continuous maximum icing conditions

Table 4 Difference rates of ice shape feature parameters for rime ice verification conditions

Difference rates (%)	Case1	Case2	Case3	Case5
X_{lowlm}	0.00997	0.0142	0.00262	1.46
X_{uplms}	0.00625	0. 0197	0.00642	4.79
X_{mw}	0.324	0.187	0.0866	5.81
X_{mt}	0.124	0.0865	0.0548	0.0214
X_{st}	8.48	1.54	5.22	0.458
Dav	1.79	0.369	1.07	2.51
Rat	11.6	5.58	15.0	12.5
1-*Par*	4.7	1.9	5.3	5.5

Table 5 Difference rates of ice shape feature parameters for glaze ice verification conditions

Difference rates (%)	Case4	Case6	Case7	Case8
X_{lowlm}	11.2	1.72	3.96	7.13
X_{uplm}	3.90	0.957	2.93	5.45
X_{mw}	14.3	0.425	8.41	13.3
X_{mt}	0.0548	1.85	0.0324	3.25
X_{st}	6.03	11.3	4.61	8.22
X_{upha}	18.4	18.6	4.84	19.3
X_{lowha}	9.58	4.28	1.92	3.48
X_{uphl}	8.61	10.2	7.00	1.86
X_{lowhl}	7.41	1.22	5.01	1.48
Dav	8.83	5.62	4.30	7.05
Rat	16.1	7.63	13.6	19.6
1-*Par*	11.0	6.2	7.1	10.8

A quantitative analysis of the icing characteristic parameters for both the predicted and simulated ice shapes was conducted. Under both continuous and intermittent maximum icing conditions, four rime ice cases and four glaze ice cases were evaluated to assess the similarity between the predicted and simulated ice shapes. Tables 4 and 5 present the differences in icing characteristic parameters for rime and glaze ice, respectively. For the rime ice cases, the predicted ice shapes exhibit a high degree of consistency with the simulated results, both in the overall and local contours. The upper and lower icing limits, as well as the icing thickness, are essentially identical between the predicted and simulated results, indicating strong predictive accuracy of the surrogate model. The *Dav* is within 4%, the *Rat* is within 15%, and the *Par* exceeds 90%. These results demonstrate strong prediction accuracy and generalization performance. For the glaze ice cases, the predicted ice shape generally aligns well with the overall simulated ice shape, though slight discrepancies are observed in the upper ice horn. The *Dav* is within 12%, the *Rat* is within 15%, and the *Par* exceeds 85%. This indicates the excellent adaptability of the rapid prediction algorithm in capturing complex glaze ice formations.

The ice shape prediction results indicate that when the ice shape is primarily governed by linear behaviour, as observed in rime ice, the surrogate model achieves high prediction accuracy, with the predicted ice shape *Par* exceeding 90%. For more complex glaze ice shapes, which exhibit significant nonlinear behaviour, the surrogate model effectively predicts the overall contour, with *Par* exceeding 85%; however, it tends to simplify intricate icing features, leading to minor local inaccuracies.

Each numerical simulation required at least 10^4 s per condition and consumed significant computational resources. In contrast, once the surrogate model was established, the icing prediction time for each condition was reduced to less than 10 s, achieving an efficiency improvement of approximately three orders of magnitude compared to numerical simulations. Although constructing the kriging surrogate model involves significant preliminary computations, once developed, it enables rapid and accurate real-time predictions of icing shapes under any given condition.

The primary error regions in the ice shape predictions by the surrogate model were observed at the ice horns, where the ice shape exhibited weak continuity, making it challenging for the model to accurately capture these variations. Shen et al. (2013) proposed increasing the number of grid points on the airfoil surface to improve the accuracy of capturing ice-corner features. Increasing the grid node density from lower to higher values enhances accuracy. However, once the grid density reaches a certain threshold, further increases do not yield significant improvements in capturing intricate icing features. For errors within the upper and lower limits, which primarily occur under glaze-ice conditions, increasing the sample size, particularly for glaze-ice samples, can help reduce these errors. Glaze ice has long been a key focus of aircraft de-icing and anti-icing research due to its sensitivity to minor variations in icing parameters. By increasing the number of glaze ice samples, the surrogate model can more accurately capture complex icing features, thereby enhancing the similarity between the predicted and simulated ice shapes.

4.3 Swept Wing Icing Prediction Model

The icing condition on a 3D swept wing is more complex than that on a straight wing because different 2D sections can exhibit varying ice shapes. This section analyses icing predictions for different 2D sections of a 3D swept wing, using the same calculation conditions as in the previous section. As shown in Fig. 13, multiple 2D sections were selected from the 3D swept-wing model to construct the corresponding rapid-icing prediction models. These sections were located at: Z=0.0b, Z=0.1b, Z=0.3b, Z=0.5b, Z=0.7b, Z=0.9b, and Z=1.0b. This totalled seven sections, each with its own prediction model. The icing data for different sections were predicted, and interpolation was performed to calculate the icing shape for any given 2D section, enabling full 3D wing icing prediction.

Figure 14 illustrates the pressure contours and streamline plots for various sections along the swept wing. Figure 15 shows the pressure coefficients for various sections along the swept wing. During aircraft flight, the wing root typically experiences higher airflow pressure, leading to complex airflow distributions that can cause boundary layer separation and turbulent regions. At the wingtip, the pressure difference between the upper and

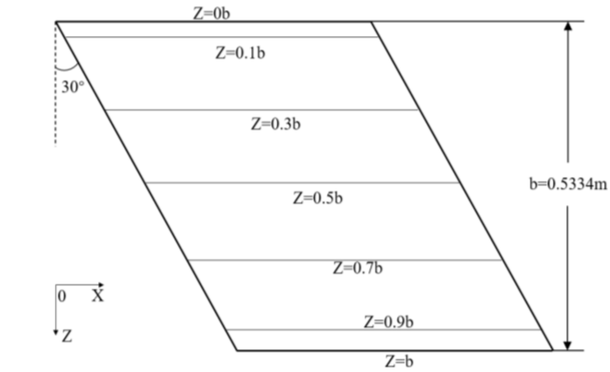

Fig. 13 Distribution of different sections of the wing

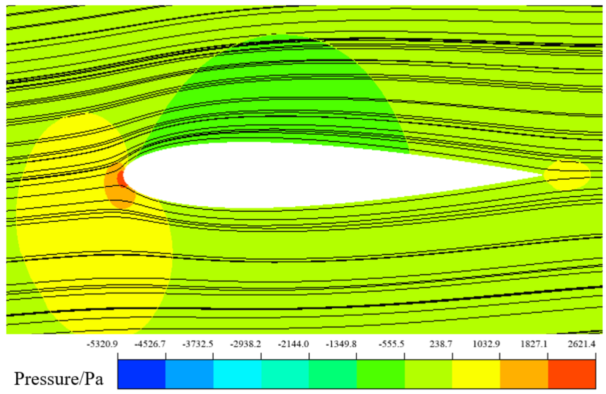

(a) Z=0.1b

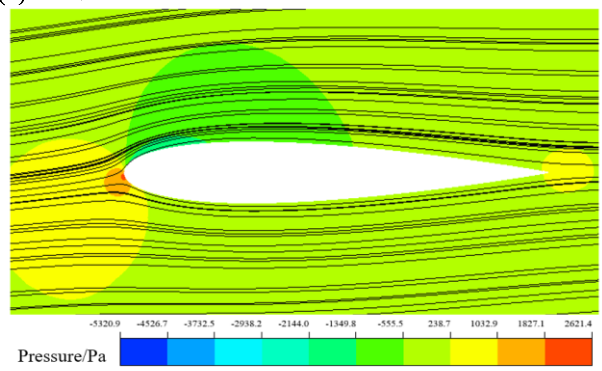

(a) Z=0.5b

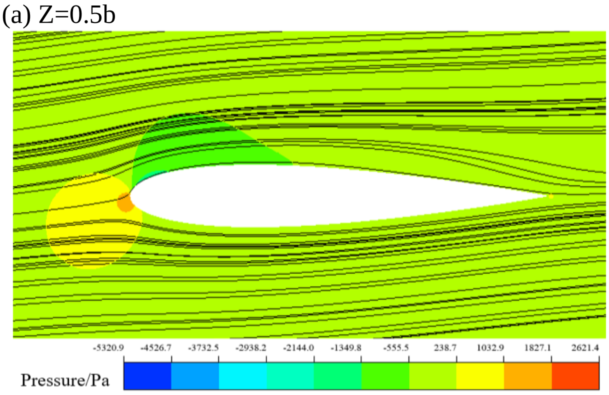

(a) Z=0.9b

Fig. 14 Contours at various positions of the wing

lower surfaces generates wingtip vortices, further affecting airflow. As a result, the airflows at the wing root and wingtip are more intricate compared to the middle sections, resulting in more complex icing shapes in these regions. Therefore, when selecting sections, the interval

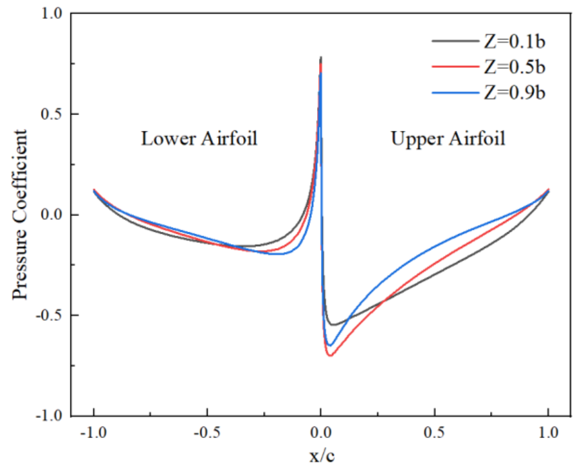

Fig. 15 Pressure coefficient at various positions of the swept wing

Table 6 Difference rate of ice shape characteristic parameters between predictions and simulations

Difference rates (%)	Z=0	Z=0.3b	Z=0.7b	Z=b
X_{lowlm}	2.05	0.197	0.647	1.80
X_{uplm}	3.38	12.8	0.119	0.332
X_{mw}	3.08	8.36	9.05	2.68
X_{mt}	7.85	3.48	2.47	5.86
X_{st}	13.0	3.50	1.17	0.619
X_{upha}	1.49	10.7	0.426	5.66
X_{lowha}	2.33	1.88	5.05	1.96
X_{uphl}	4.50	18.2	13.5	0.969
X_{lowhl}	3.40	6.44	6.95	0.717
Dav	4.56	7.28	4.38	2.29
Rat	10.4	9.73	9.50	19.6
1-*Par*	6.3	8.0	5.9	7.5

near the root and tip sections is set to 0.1 times the wingspan, while the interval in the middle of the wing is set to 0.2 times the wingspan. As glaze ice exhibits more complex structures and better represents the predictive capability of the surrogate model, the icing parameters for glaze ice Case 7 were selected for the 3D icing prediction.

Figure 16 presents the comparison between simulated and predicted ice shapes for selected sections under glaze ice conditions. Specifically, it illustrates ice shape comparisons at sections Z=0.0b, Z=0.3b, Z=0.7b, and Z=1.0b, respectively. The results demonstrate a strong agreement between the ice shapes predicted by the surrogate model and those obtained from numerical simulations. Table 6 presents the discrepancy rates of ice shape characteristic parameters between the surrogate model predictions and numerical simulations across different sections. Overall, the ice shapes at the four sections exhibit a high degree of consistency. The ranges from 9% to 20%, while the remains above 90% for all cases. The upper and lower limit positions, ice horn horns, and stagnation point ice thickness all demonstrate good consistency. However, a noticeable discrepancy is observed in the ice horn length at the midsection of the airfoil, with a characteristic difference rate of approximately

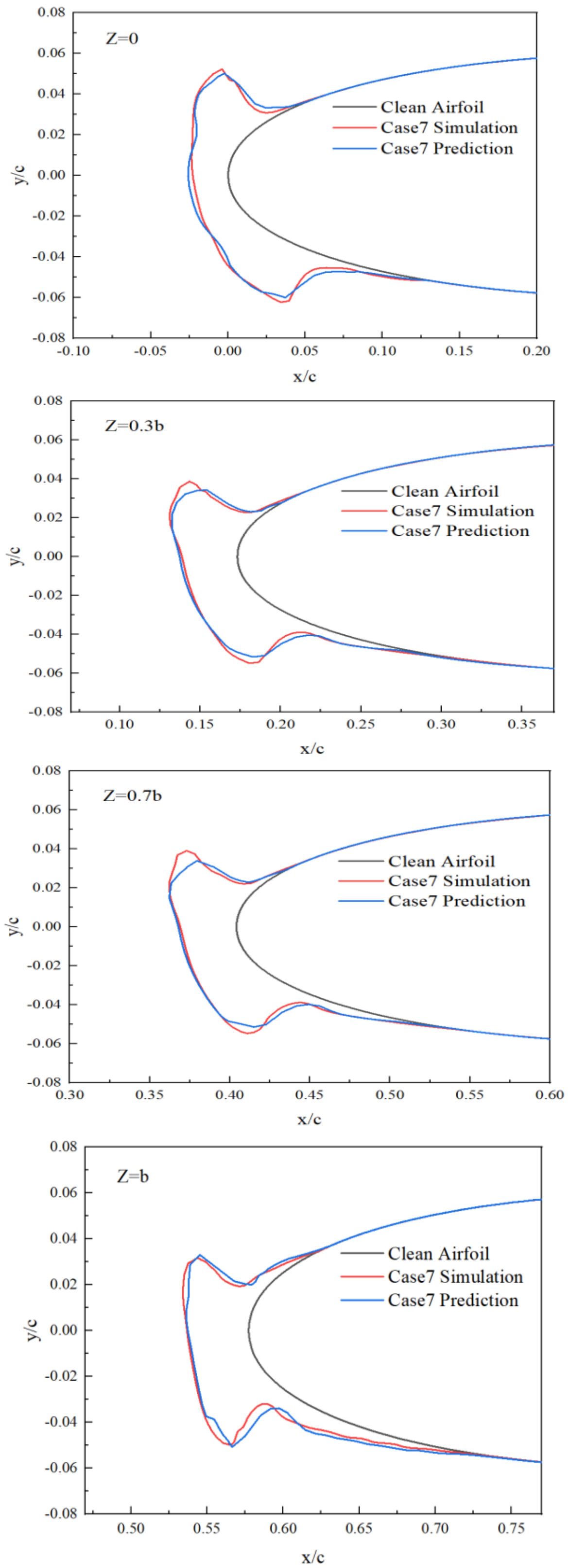

Fig. 16 Comparison of numerically simulated ice shapes and surrogate model ice shapes for selected sections

15%. Despite this, the predicted ice shapes across different sections align well with the simulated ice shapes, indicating the surrogate model's good prediction performance.

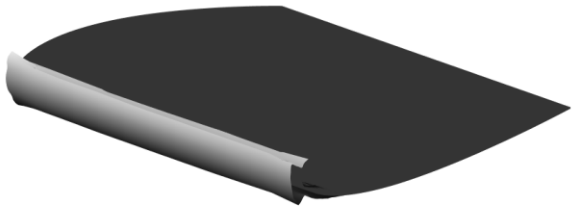

(a) 3D predicted ice shape

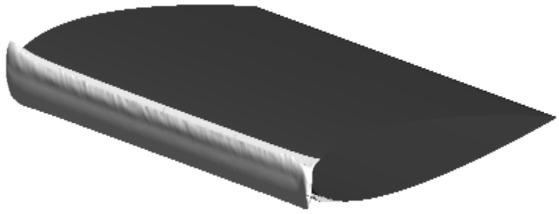

(b) Simulated ice shape

Fig. 17 Comparison of 3D predicted and simulated ice shape

After developing surrogate models for seven distinct sections, the predicted ice shapes were obtained under validation conditions. To construct a comprehensive 3D ice shape, uniform interpolation was applied to generate ice shapes for 100 sections along the spanwise direction. As shown in Fig. 17, the 3D predicted ice shape closely aligns with the numerically simulated ice shape, effectively illustrating the ice accretion process from the wing root to the tip. In the 3D predicted ice shape, two sections at Z=0.375b and Z=0.768b were selected for comparison with the numerically simulated ice shape, as shown in Fig. 18, which closely align with the overall contour obtained from numerical simulations.

Table 7 presents the discrepancies in ice shape characteristic parameters between the predicted and simulated results. The interpolated predicted ice shapes for both sections exhibit a high degree of overlap with the numerical simulations, demonstrating general consistency in the upper and lower limits, ice horn lengths, and stagnation ice thicknesses. Only the length of the upper ice horn exhibited a relative error of 15%. The was approximately 6%, and the Par was above 92%. These results indicate that constructing a 3D prediction model using interpolation algorithms based on multiple 2D section surrogate models effectively predicts the 3D ice shape. By averaging the ice shape similarity across multiple 2D sections, the overall 3D ice shape similarity was determined. The similarity between the surrogate model prediction and the numerical simulation for the entire 3D ice shape exceeded 90%.

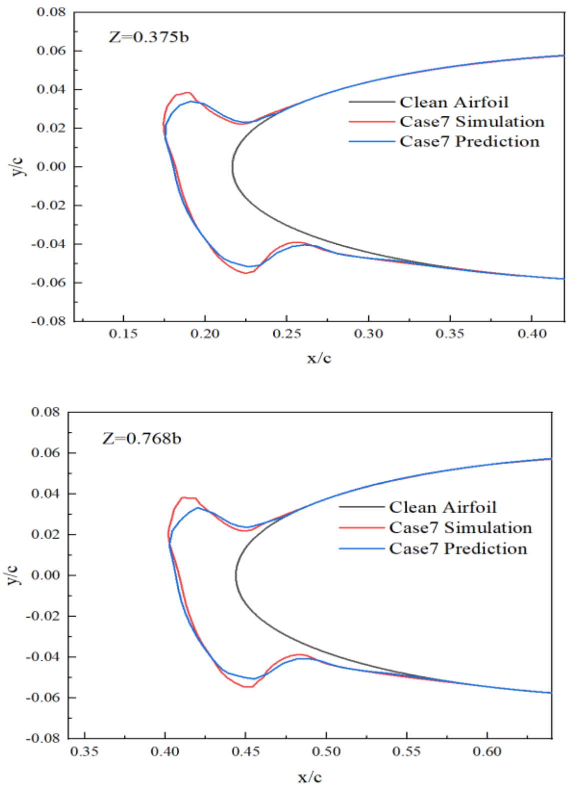

Fig. 18 Comparison of ice shape predicted by interpolation algorithm and numerical simulation

Table 7 Difference rate of ice shape between uniform interpolation algorithm and simulations

Difference rates (%)	Z=0.375b	Z=0.768b
X_{lowlm}	3.56	0.695
X_{uplm}	3.97	1.15
X_{mw}	6.95	9.44
X_{mt}	3.86	4.26
X_{st}	1.45	6.13
X_{upha}	7.54	6.44
X_{lowha}	3.74	1.03
X_{uphl}	14.4	17.1
X_{lowhl}	6.27	7.36
Dav	5.75	5.96
Rat	9.27	10.2
1-*Par*	6.8	7.2

5. CONCLUSIONS

A rapid prediction algorithm utilising POD and Kriging was proposed to efficiently and accurately predict ice shapes on swept wings. To establish a comprehensive icing dataset, 120 icing conditions were generated using the OLHS method, considering five key physical parameters under both continuous and intermittent maximum icing conditions. Numerical simulations were conducted for these conditions, enabling the construction of two-dimensional airfoil surrogate models. Finally, uniform interpolation was employed to predict the 3D airfoil icing shape. The key findings of this study are as follows:

(1) The surrogate model effectively predicts both the ice shape and its characteristic parameters, achieving a *Par* value exceeding 90% for rime ice and 85% for glaze ice. While Minor deviations were observed in the predicted ice horn and icing limit positions, the overall agreement with numerical simulations remained strong.

(2) Analysis of the icing parameters revealed that flight speed and LWC primarily influenced the icing rate, ice horn formation, and stagnation point thickness. MVD significantly affected the icing rate, ice horn development, and upper and lower icing limits. Ambient temperature primarily influenced the ice horn shape and stagnation point thickness.

(3) The surrogate model achieved a computational efficiency improvement of three orders of magnitude compared to traditional numerical simulations. Once constructed, it enables the fast and accurate real-time prediction of icing shapes for any condition.

(4) The 3D ice shape prediction, derived by interpolating the surrogate model predictions across multiple sections, closely aligned with numerical simulation results. This demonstrates the predictive capability of the proposed method for accurately modelling 3D airfoil icing.

ACKNOWLEDGEMENTS

This work was supported by National Key R&D Program of China (Grant No.2021YFB2601700), the Fundamental Research Funds for the Central Universities (Grant No. 25CAFUC03011), the CAAC Key Laboratory of Flight Techniques and Flight Safety (Grant No. F2024KF15C) and the Civil Aviation Flight University of China Science Innovation Fund for Graduate Students (Grant No. 24CAFUC10207).

CONFLICT OF INTEREST

There is no conflict of interest to disclose.

AUTHORS CONTRIBUTION

Guo Qilei guided the research, designed the article structure. **Du Jie** designed the study, complied the models, and wrote the manuscript. **Cheng Han** and **Yue Yuan** contributed to the analysis of the model and background of the study. **Ma Yao** contributed to data and preparation of draft and figures. All authors commented on the manuscript draft and approved the submission.

REFERENCES

Abdelghany, E. S., Farghaly, M. B., Almalki, M. M., Sarhan, H. H., Essa, M. E. S. M. (2023). Machine learning and iot trends for intelligent prediction of aircraft wing anti-icing system temperature. Aerospace, *10*, 676. https://doi.org/10.3390/aerospace10080676

Aliaga, C, N., Aube, M, S., Baruzzi, G, S., & Habashi, W, G. (2011). Fensap-ice-unsteady: unified in-flight icing simulation methodology for aircraft rotorcraft and jet engines. *Journal of Aircraft*, *48*(1), 119-126. https://doi.org/10.2514/1.C000327

Appiah, K. P., Martos, B., Atuahene, I., & William, S. V. (2013). *U.S. inflight icing accidents and incidents, 2006 to 2010*. Industrial & Systems Engineering Research Conference A Krishnamurthy & Wkv Chan.

Bourgault, Y., Beaugendre, H., & Habashi, W. G. (2000). Development of a shallow-water icing model in fensap-ice. *Journal of Aircraft, 37*(4), 640-646. https://doi.org/10.2514/2.2646.

Bourgault, Y., Habashi, W. G., Dompierre, J., & Baruzzi, G. S., (1999). A Finite element method study of eulerian droplets impingement models. *International Journal for Numerical Methods in Fluids, 29*(4), 429-449. https://doi.org/10.1002/(SICI)1097-0363(19990228)29:4<429::AID-FLD795>3.0.CO;2-F

Bu, X., Yang, R., Yu, J., Shen, X., & Lin, G. (2017). Fast algorithm for prediction of airfoil anti-icing heat load. *Energy and Power Engineering, 5*, 493-497. https://doi.org/10.4236/epe.2013.54B095

Chang, S., Leng, M., Wu, H., & Thompson, J. (2016). Aircraft ice accretion prediction using neural network and wavelet packet transform. *Aircraft Engineering and Aerospace Technology: An International Journal, 88*(1), 128-136. https://doi.org/10.1108/AEAT-05-2014-0057

Civil Aviation Administration of China. (2011). CCAR25 transport category aircraft certification standards.

Dai, H., Zhu, C. L., Zhao, H. Y., & Liu, S. Y. (2021). A new ice accretion model for aircraft icing based on phase-field method. *Applied Sciences, 11*(12), 5693. https://doi.org/10.3390/app11125693

European Union Aviation Safety Agency. (2016). Certification specifications and acceptable means of conmpliance for large aeroplanes.

Federal Aviation Administration. (2004). Certification of transport category airplanes for flight in icing conditions: FAA AC25.1419-1A.

Forrester, A., Sobester, A., & Keane, A. (2008). *Engineering design via surrogate modelling: a practical guide*. DBLP.

Fortin, G., Laforte, J. L., & Ilinca, A. (2006). Heat and mass transfer during ice accretion on aircraft wings with an improved roughness model. *International Journal of Thermal Sciences, 45*(6), 595-606. https://doi.org/10.1016/j.ijthermalsci.2005.07.006

Habashi, W. G., Morency, F., & Beaugendre, H. (2003). *FENSAP-ICE: A second generation 3D CFD-based in-flight icing simulation system*. SAE Technical Paper Series. https://doi.org/10.4271/2003-01-2157

Han, Z. H. (2016). Kriging surrogate model and its application to design optimization： A review of recent progress. *Acta Aeronautica et Astronautica Sinica, 37*(11), 3197-3225.

https://doi.org/10.1007/s12206-011-0118-4

Jung, S. K., Shin, S., Myong, R. S., & Cho, T. H. (2011). An efficient CFD-based method for aircraft icing simulation using a reduced order model. Journal of Mechanical Science & Technology, 25(3): 703-711. https://doi.org/10.1007/s12206-011-0118-4

Kim, H., & Bragg, M. (1999). *Effects of leading-edge ice accretion geometry on airfoil performance*. Proceedings of the 17th Applied Aerodynamics Conference, AIAA-1999-3150. https://arc.aiaa.org/doi/pdf/10.2514/6.1999-3150

Li, B., Sun, Q., Xiao, D., & Zhang, W. (2022). Numerical Investigation of the Aerofoil Aerodynamics with Surface Heating for Anti-Icing. *Aerospace, 9*, 338. https://doi.org/10.3390/aerospace9070338

Li, S., Qin, J., He, M., & Paoli, R. (2020). Fast evaluation of aircraft icing severity using machine learning based on XGBoost. *Aerospace, 7*(4), 36. https://doi:10.3390/aerospace7040036

Lin, G, P., Bu, X, Q., & Shen, X, B. (2015). *Aircraft icing and anti icing technology*. Beijing University of Aeronautics and Astronautics Press. https://isbn.org/9787512420182

Liu, T., Dong, L., Huang, R. (2019). Iceshape prediction method of aero-icing based on reduced order model. *Journal of Beijing University of Aeronautics and Astronautics*, *45*(5), 1033-1041.

Milani, Z, R., Matida, E., Razavi, F., Sultana, K, R., Patterson, T., Nichrman, L., Benmeddour A., & Bala, K. (2024). Numerical icing simulations of cylindrical geometry and comparisons to flight test results. *Journal of Aircraft, 61*(4), 1272-1282. https://doi.org/10.2514/1.C037682

Min, G., & Jiang, N. (2024). Flow fields prediction for data-driven model of parallel twin cylinders based on pod-rbfnn and pod-bpnn surrogate models. *Annals of Nuclear Energy, 199*(5), 1.1-1.22. https://doi.org/10.1016/j.anucene.2024.110342

Niu, J., Sang, W., & Li, D. (2023). Fast prediction of multiple parameters related to iced airfoil based on POD and kriging methods. *Journal of Applied Fluid Mechanics*, 325-336. https://doi.org/10.47176/jafm.16.02.1379

Olejniczak, D., & Nowacki, M. (2018). Evaluation of the influence of icing on wings on aircraft flight parameters. *Transportation Research Procedia, 35*(3), 100-109. https://doi.org/10.1016/j.trpro.2018.12.017

Olsen, W., Shaw, R. J., & Newton, J. (1984*). Ice shapes and the resulting drag increase for a NACA 0012 airfoil*. Proceedings of the 22nd Aerospace Sciences Meeting, AIAA-1984-0109. https://arc.aiaa.org/doi/pdf/10.2514/6.1984-109

Pellissier, M. C., Habashi, W. G., & Pueyo, A. (2012). Optimization via FENSAP-ICE of aircraft hot-air anti-icing systems. *Journal of Aircraft*, *48*(1), 265-276. https://doi.org/10.2514/1.C031095

Qiu, Y, S., Bai, J, Q., & Hua, J. (2013). Flow field estimation method based on proper orthogonal decomposition and surrogate model. *Acta Aeronautica et Astronautica Sinica*, *34* (6), 1249-1260. https://doi.org/10.7527/S1000-6893.2013.0229

Ruff, G. A., & Anderson, D. N. (2003). *Quantification of ice accretions for icing scaling evaluations.* 36th AIAA Aerospace Sciences Meeting and Exhibit. AIAA-98-0195. https://doi.org/10.2514/6.1998-195

Ryley, T., Baumeister, S., & Coulter, L. (2020). Climate change influences on aviation: a literature review. *Transport Policy*, *92*. https://doi.org/10.1016/j.tranpol.2020.04.010

Shen, X., Yu, J., & Lin, G. (2013). Fast prediction of ice shape based on proper orthogonal decomposition method. *Journal of Aerospace Power*, *28*(4) 807-812. https://doi.org/10.13224/j.cnki.jasp.2013.04.015

Shin, J., & Bond T. (1992). *Results of an icing test on a NACA 0012 airfoil in the NASA Lewis icing research tunnel.* 30th Aerospace Sciences Meeting and Exhibit. AIAA-92-0647. https://doi.org/10.2514/6.1992-647

Sirovich, L. (1987). Turbulence and the dynamics of coherent structures III： Dynamics and scaling. *Quarterly of Applied Mathematics*, *45* (3), 583-590. https://doi.org/10.1090/qam/910462

Suo, W., Sun, X., Zhang, W., & Yi, X. (2024). Aircraft ice accretion prediction based on geometrical constraints enhancement neural networks. *International Journal of Numerical Methods for Heat & Fluid Flow*, *34*(9), 3542-3568. https://doi.org/10.1108/HFF-01-2024-0019

Yi, X., Wang, Q., Chai C., & Guo, L. (2021). Prediction model of aircraft icing based on deep neural network. *Transactions of Nanjing University of Aeronautics and Astronautics*, *38*(04):535-544. https://doi.org/10.16356/j.1005-1120.2021.04.001

Yi, X. (2007). Numerical computation of aircraft icing and study on icing test scaling law. *China Aerodynamics Research and Development Center*, *2007*.

Zhao, H., Gao, Z. H., & Xia, L. (2022). Efficient aerodynamic analysis and optimization under uncertainty using multi-fidelity polynomial chaos-kriging surrogate model. *Computers & Fluids*. https://doi.org/10.1016/j.compfluid.2022.105643

Zhou, Z. H., Yi, X., & Guo, L. (2016). Quantitative method for ice accretions comparison. *Acta Aerodynamica Sinica*, *34* (5), 556-561. https://doi.org/10.7638/kqdlxxb-2015.0221